IMAGE-BASED STUDY OF BREAKING AND BROKEN WAVE CHARACTERISTICS IN FRONT OF THE SEAWALL

Weijie Liu[1] and Yoshimitsu Tajima[1]

This study aims to study the breaking and broken wave characteristics in front of the vertical seawall. Laboratory experiments were performed to represent such phenomena. A physical model of a vertical seawall installed on the mild slope was made in the wave flume. Image-based measuring technique was developed and applied to capture the wave characteristics as high-resolution data sets both in spatial and temporal domains. By analyzing the high-resolution data, behaviors of partial standing waves were successfully captured in front of the seawall. Comparisons of obtained data with and without seawall clearly showed the difference in cross-shore distributions of wave height, mean water level and skewness while no clear difference was observed in asymmetry. Obtained experimental data was then used to validate the applicability of Boussinesq wave model attached with existing breaking models. It was found that both viscosity-type and surface roller-type breaking models tended to overestimate the energy dissipation in front of the seawall.

Keywords: breaking and broken waves; partial standing waves; breaking wave models

INTRODUCTION

Coastal structures such as seawalls have been widely used for shore and harbor protections. Waves are reflected by those structures and form complex partial standing waves. Predictive skills of such complex wave field in the vicinity of the coastal structure are essential for better evaluations of the surrounding scour and erosion. Boussinesq-type time-resolving non-linear dispersive wave models are widely used for computations of such relatively complex wave field. Introducing appropriate breaking and broken wave model, these models can accommodate computations of breaking and broken wave field near the shore. Most of existing breaking wave models, however, are mainly based on the assumptions of progressive waves and thus applicability of these models to partial standing wave field is still unclear. In addition, most models are tested against measured broken wave height but not against other features such as surface water profiles, which may have significant influence on net sediment transport rate.

This study focuses on such breaking and broken wave characteristics in front of a vertical seawall and aims to obtain image-based high-resolution data sets of surface water fluctuations through the series of laboratory experiments. Obtained experimental data is also used to check the applicability of existing breaking models under partial standing wave field.

LABORATORY EXPERIMENT

Laboratory experiments was first performed to investigate the characteristics of breaking and broken waves in front of a vertical seawall in the 2D wave flume, which is 30m long and 60cm wide with transparent glass side walls mounted in steel frame.

Basic Experimental Setups

Fig.1 shows the basic experimental setups of the present laboratory experiments. As seen in the figure, a 1:30 sloping beach was made starting at around 12m from the wave maker in the wave flume. A vertical solid wall as a vertical seawall, which is widely used around the world as shore protection structures and as quay walls in harbors, was installed on the 1/30 slope and its horizontal distance from the wave maker is 19.795m. In order to capture all the information of characteristics of breaking and broken waves in front of the vertical seawall, image-based measuring system was developed and applied to capture the wave characteristics with high resolutions both in time and space domains. Two video cameras were used to record successive still images of the instantaneous water surface boundary along the cross section of about 2m (2 steel frames of the wave flume) in front of the seawall in which the water and background were colored in blue and yellow, respectively. To ensure the high resolution of images, JVC HD cameras were used instead of high speed camera. Two spotlights were used to light up the measuring area. In order to synchronize two cameras, spotlights were turned off just before stopping the video recording in each experimental case.

[1]Department of Civil Engineering, The University of Tokyo, Hongo 7-3-1, Bunkyo-ku, Tokyo 113-8656, Japan

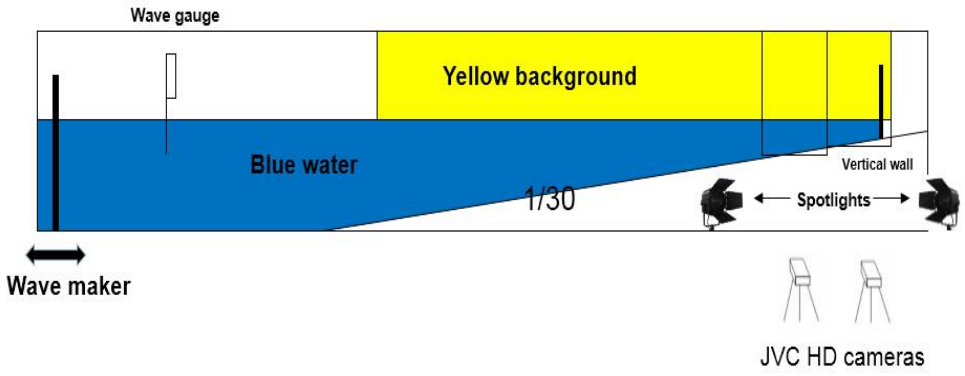

Figure 1. Basic experimental setups of the present laboratory experiments

Ground Control Points

In order to preform image-based analysis, which will be specified later, after setting the basic experimental setups, Ground Control Points (GCP) which determine the geometric relationships between actual XY-coordinates and image pixel coordinates should be made as reference points. Fig.2 shows the full sketch of all the GCP with known positions on the side glass of the wave flume where surface water boundary were recorded by the cameras. Eight Ground Control Points in two horizontal lines were made in one frame and the positions of GCP on the side glass are specified. If the actual XY-coordinate system is determined on the side glass, then the actual XY-coordinates of GCP can be easily obtained. For clear distinction in the image, yellow tape was used in the blue water and dark area and red tape was used in the yellow background area.

Image-based Analysis

Image rectification. After recording the water surface fluctuations using the JVC HD cameras, videos were converted to still images of each frame. Obtained still images was first rectified due to the distortion of the camera lens before starting the analysis process. Based on the Ground Control Points specified before and the distortion coefficients calculated by 12 bench-mark points on a graph sheet, rectification parameters such as camera locations, angles, focal length and lens distortion, were estimated so that the obtained parameters yield the minimum root-mean-square errors of estimated pixel coordinates at GCP (Tajima and Sato, 2010).

Air-water boundary detection. The Air-Water boundary detection in the image-based measuring system is the detection of the sudden pixel RGB values change from background to the water threshold in the extracted still images.Based on the RGB values in each pixel, the surface water boundary was detected by the following parameter:

$$A = R + G - B \qquad (1)$$

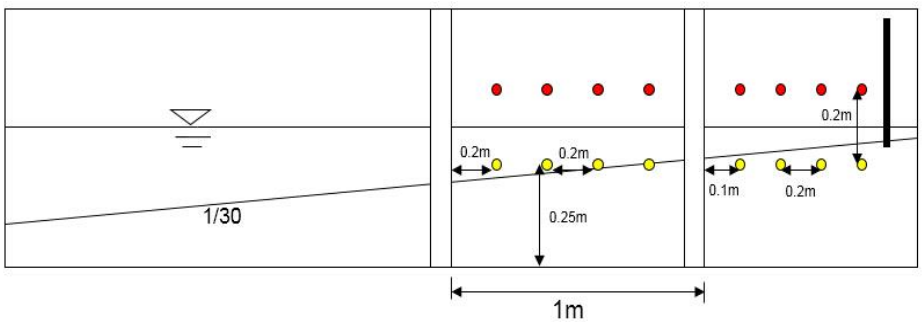

Figure 2. Full sketch of all the GCP with known distance on the side glass of the wave flume where surface water boundary were recorded by the cameras

Since yellow is represented by larger values of both R and G and blue, on the other hand, is represented by larger B and smaller R and G, A should give a large value in the yellow background and smaller value on the blue water and should be decreased abruptly at the air-water boundary. Fig.3 shows a typical snapshot of the wave propagation and breaking on the 1/30 slope. Since the observed fluctuating range of the surface water boundary is within the range as two horizontal red pixel lines indicate in the figure, searching area for the air-water boundary detection is just limited within this effective range. Also this limited searching area can exclude the influence of the Ground Control points made by the yellow and red tapes. Fig.4 shows the downward vertical distribution of A along the vertical pixel line TT within the searching area as indicated in Fig.3. As seen in Fig.3, there is an abrupt decrease of A even at the surface of broken waves where the water color tended to be brighter than deep water. Under the present experimental setup, A was always greater than 200 on the yellow background while it was always less than 100.Then this study set the surface water boundary condition of A by a single critical value, A = 150. The system searches the pixel location in the vertical downward direction where A first goes below the critical value and the detected pixel coordinates were then transferred to the rectified XY-coordinates based on the obtained rectification parameters in advance. Estimated error of the rectified coordinates of the still water level, which are defined to be zero for the present rectification, was less than 1mm.

Fig.5 compares the time-varying surface water fluctuations estimated by the present image-based

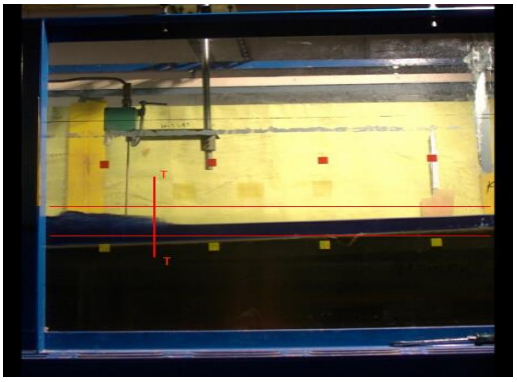

Figure 3. A typical snapshot of the wave propagation and breaking on the 1/30 slope

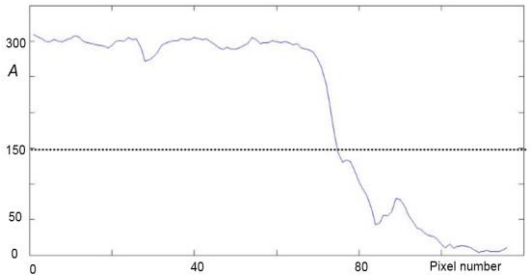

Figure 4. Downward vertical distribution of A along the vertical pixel line TT within the searching area as indicated in Fig.3

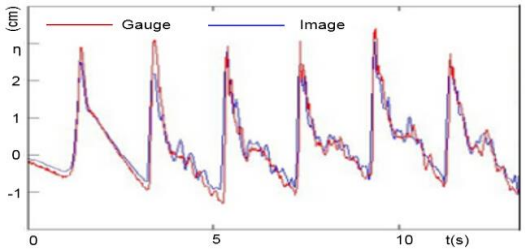

Figure 5. Comparisons of time-varying surface water fluctuations estimated by the present image-based measuring system and the ones measured by the wave gauge

measuring system and the ones measured by the wave gauge. It clearly shows that, even under the breaking wave, the image-based system is able to capture overall surface fluctuations within acceptable errors.

Experimental Wave Cases

Table 1 enlists the experimental wave cases and conditions. In the table, *Ti* is the incident wave height, *ho* is the water depth near wave maker over the horizontal bottom and *Hi* is the incident wave height. Five typical regular wave cases were introduced and incident wave conditions and water depth near the wave maker were selected respectively in each of experimental cases.

For case 1, progressive waves with the same incident wave conditions were also performed in this study without the presence of seawall on the slope. The comparison between the case with seawall and the one without seawall may provide better understanding of the influence of the vertical seawall and the characteristics of breaking and broken waves under partial standing wave filed in this study.

Table 1. List of experimental wave conditions, "P" indicates that the same incident waves were introduced to the same sloping beach but without vertical seawall.

Case	*Ti* (s)	*ho*(cm)	*Hi* (cm)	Remarks
1	1.2	30	4.8	P
2	1.4	30	4.4	
3	1.6	30	4.2	
4	1.2	31.5	5.5	
5	1.6	31.5	5.1	

Results and Discussions

Fig.6 (a) shows the time-spatial distributions of extracted surface water level for Case 1. This figure shows the surface water level for 30s starting from the first wave generated from wave maker was captured by the camera. Fig.6 (b) and (c) show the standard deviation of the surface water fluctuations (Std.) and mean water level for Case 1. Std. and mean water level were computed based on the extracted surface water level data of each single wave period so that time-variation of these values as waves propagate, break, hit the seawall and finally form partial standing waves can be observed. In Fig.6, origin of the horizontal axis is set at the location of seawall and the vertical axis is time. As seen in Fig.6, antinodes of standing wave features can be clearly observed at three locations, around X= -35cm, -80cm and -130cm.

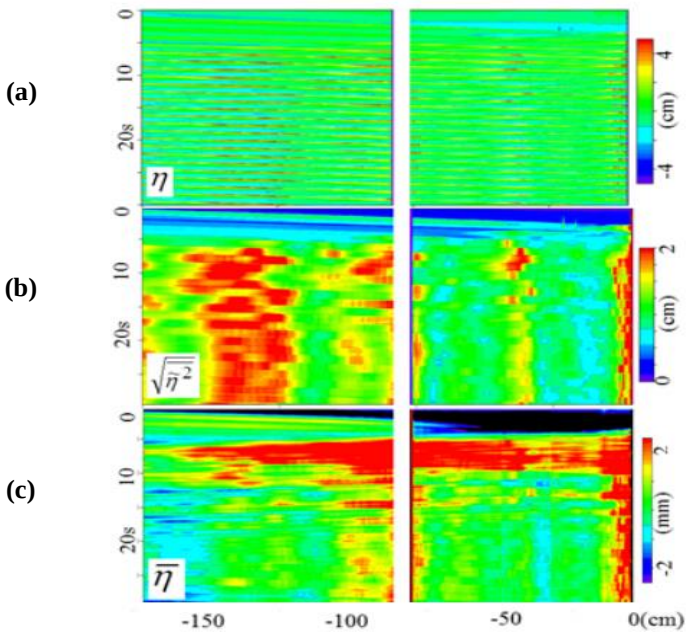

Figure 6. Time-spatial distributions of (a) extracted surface water level, (b) standard deviation of the surface water fluctuations and (c) mean water level for Case 1

Fig.7 shows the cross-shore distributions of (a) Std. and (b) mean water level at every 1/30s around t=20sec for one wave period when these values nearly reach to equilibrium state for Case 1. As seen in this figure, the mean water level had peaks at antinodes and also where standard deviations of surface water fluctuations had higher peaks. However, other high peaks were also observed between antinodes.

Fig.8 shows the time-variation of (a) standard deviation (Std.), (b) mean water level, (c) skewness (blue) and asymmetry (red) of fluctuating water level at X=-35cm where the first antinode of partial standing waves was observed for case 1. In the figure, each of these values were computed over one-wave period around the arbitrary time so that one can clearly see how these values change with time. As seen in this figure, mean water level was rapidly elevated at the beginning and then go down to reach equilibrium state. This decrease of the mean water level may be due to formation of partial standing waves. While asymmetry was stable, skewness showed significant fluctuations even after the formation of partial standing waves.

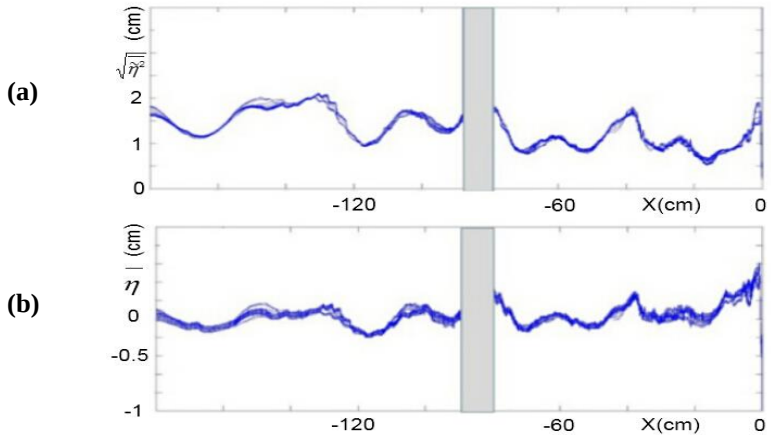

Figure 7. Cross-shore distributions of (a) std. and (b) mean water level at every 1/30s around t=20sec for one wave period for Case 1

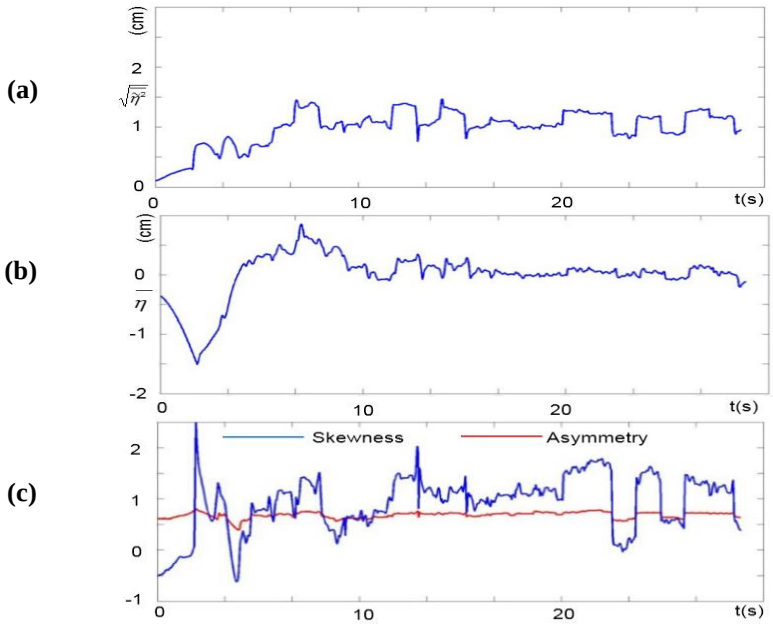

Figure 8. Time-variation of (a) Std., (b) mean water level, (c) skewness (blue) and asymmetry (red) of fluctuating water level at X=-35cm where the first antinode of partial standing waves was observed for Case 1

Fig.9 to Fig. 20 show the similar results obtained for other cases performed in the present image-based study. The primary difference among these different wave cases was the cross-shore locations of antinodes

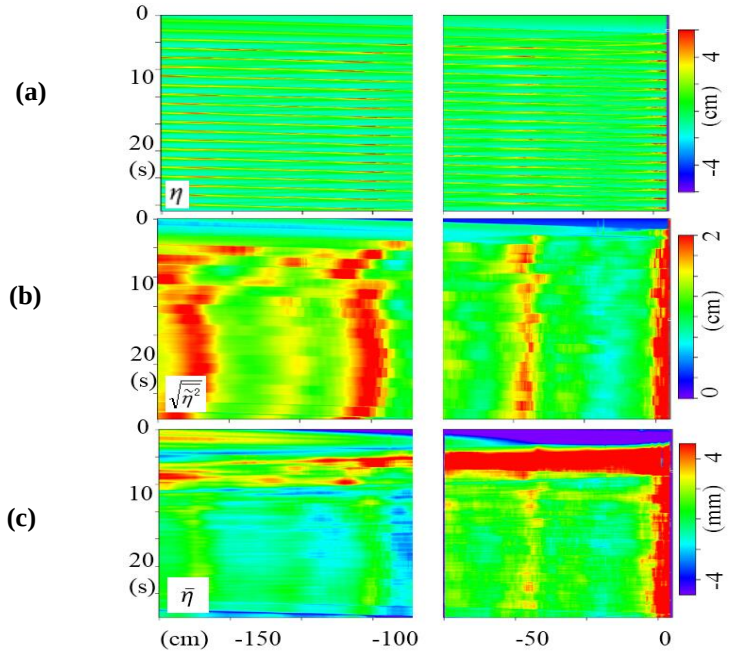

Figure 9. Time-spatial distributions of (a) extracted surface water level, (b) standard deviation of the surface water fluctuations and (c) mean water level for Case 2

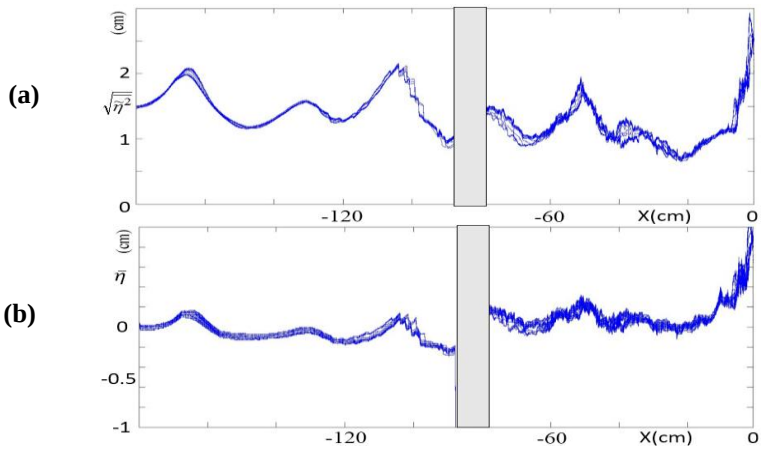

Figure 10. Cross-shore distributions of (a) std. and (b) mean water level at every 1/30s around t=20sec for one wave period for Case 2

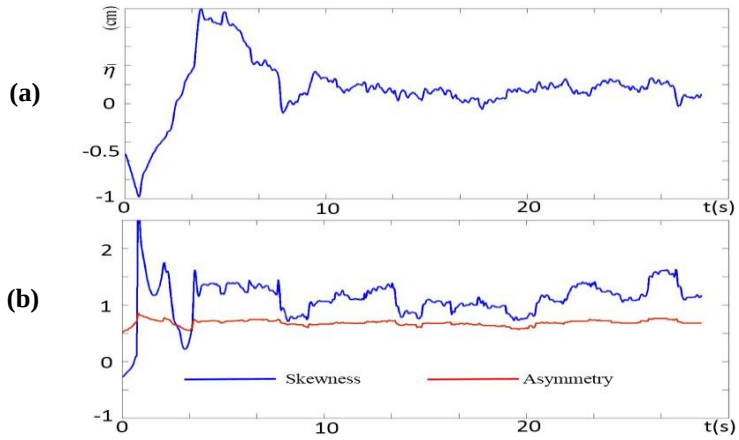

Figure 11. Time-variation of (a) mean water level, (b) skewness (blue) and asymmetry (red) of fluctuating water level at X=-50cm where the first antinode of partial standing waves was observed for Case 2

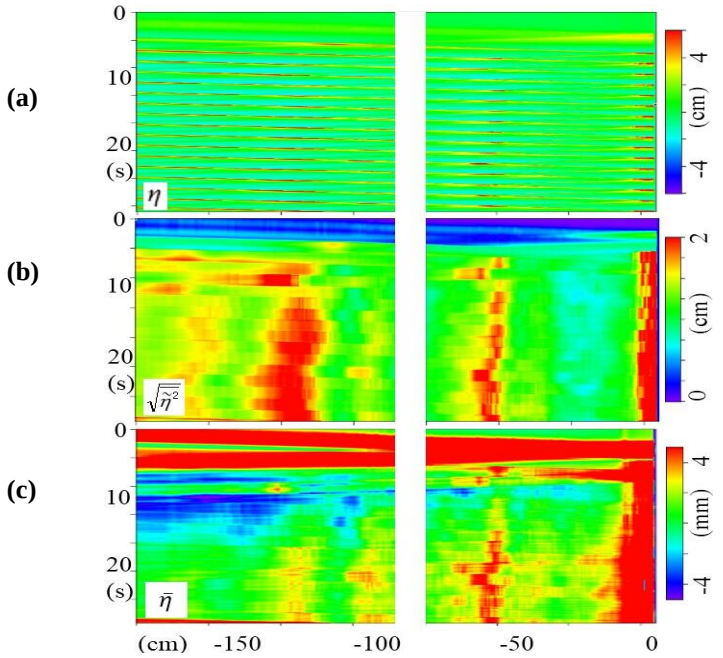

Figure 12. Time-spatial distributions of (a) extracted surface water level, (b) standard deviation of the surface water fluctuations and (c) mean water level for Case 3

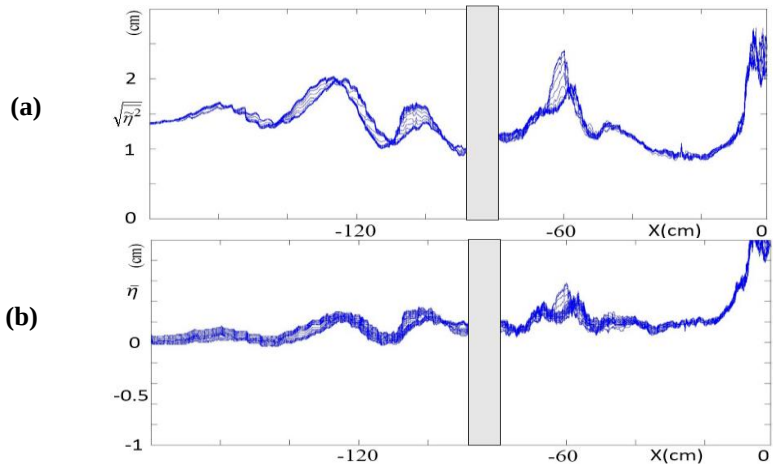

Figure 13. Cross-shore distributions of (a) std. and (b) mean water level at every 1/30s around t=20sec for one wave period for Case 3

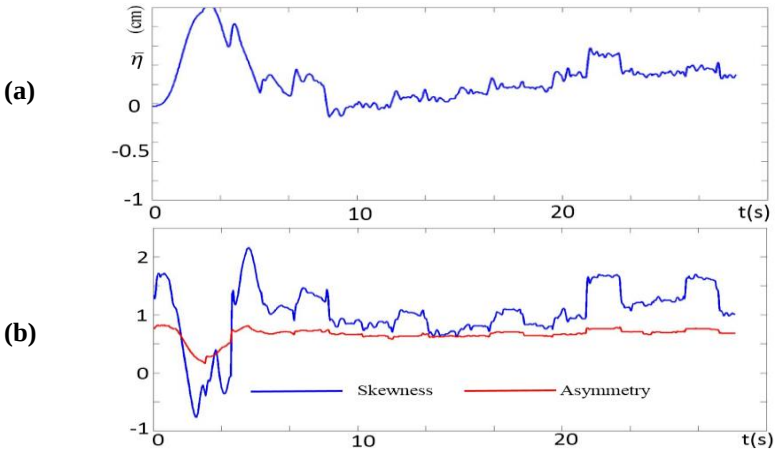

Figure 14. Time-variation of (a) mean water level, (b) skewness (blue) and asymmetry (red) of fluctuating water level at X=-60cm where the first antinode of partial standing waves was observed for Case 3

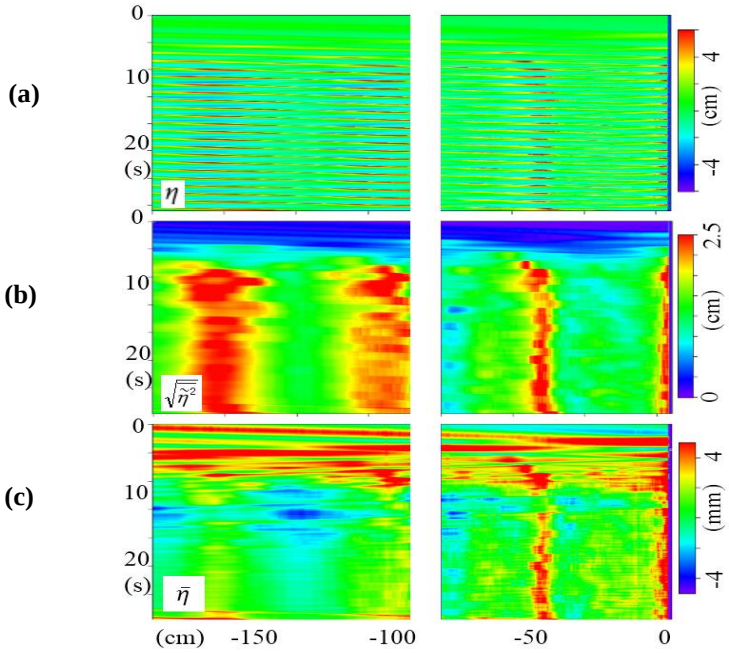

Figure 15. Time-spatial distributions of (a) extracted surface water level, (b) standard deviation of the surface water fluctuations and (c) mean water level for Case 4

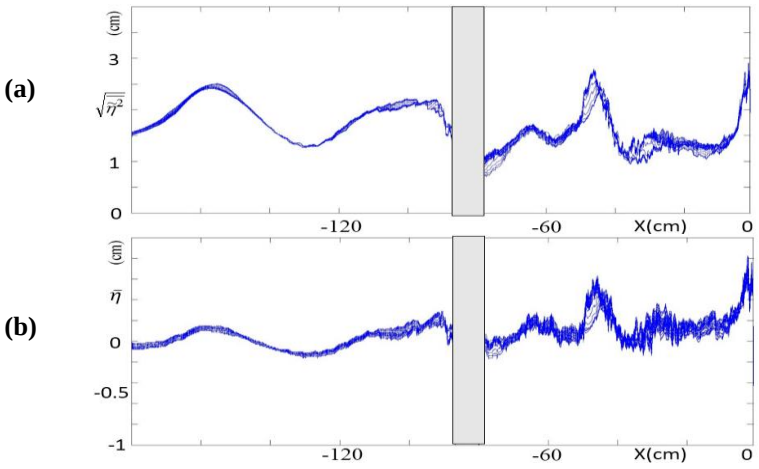

Figure 16. Cross-shore distributions of (a) std. and (b) mean water level at every 1/30s around t=20sec for one wave period for Case 4

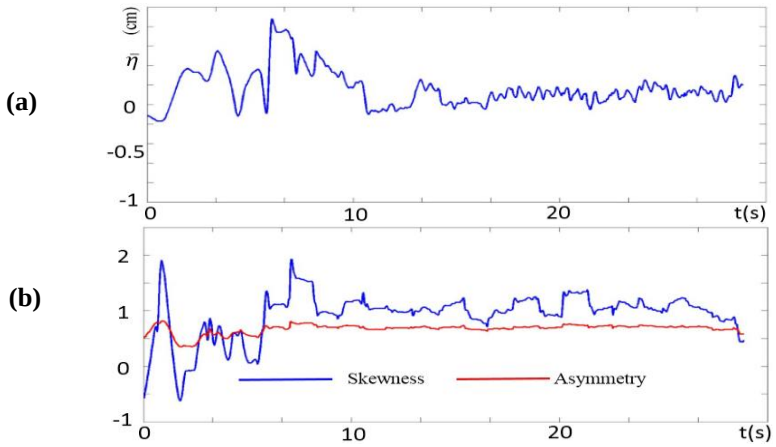

Figure 17. Time-variation of mean water level(top), skewness (blue) and asymmetry (red) of fluctuating water level(bottom) at X=-45cm where the first antinode of partial standing waves was observed for Case 4

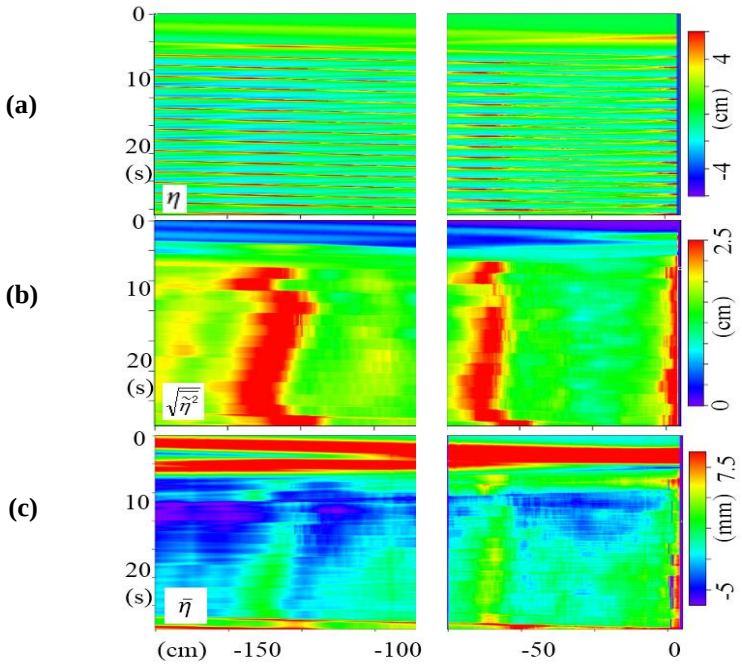

Figure 18. Time-spatial distributions of (a) extracted surface water level, (b) standard deviation of the surface water fluctuations and (c) mean water level for Case 5

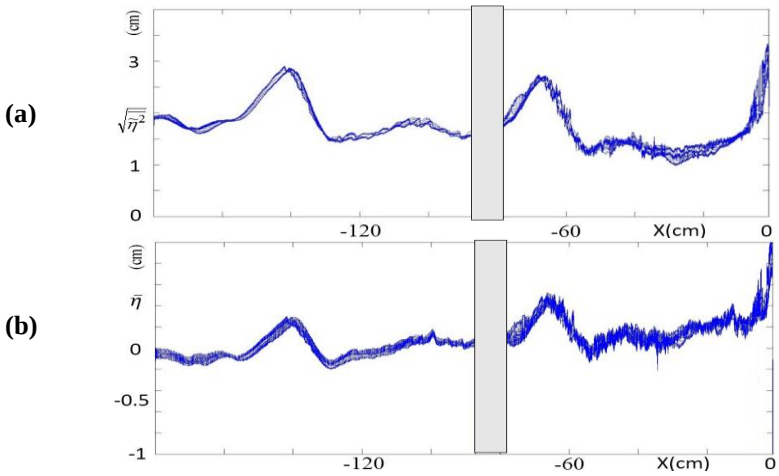

Figure 19. Cross-shore distributions of (a) std. and (b) mean water level at every 1/30s around t=20sec for one wave period for Case 5

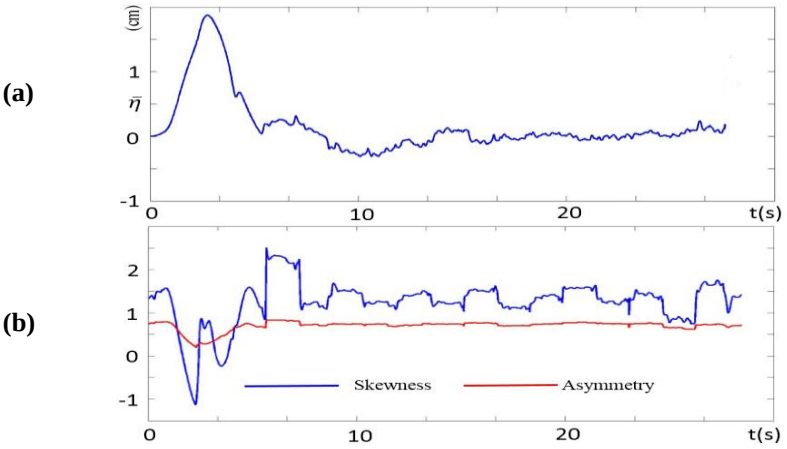

Figure 20. Time-variation of mean water level(top), skewness (blue) and asymmetry (red) of fluctuating water level(bottom) at X=-65cm where the first antinode of partial standing waves was observed for Case 5

Further comparison was made between Case 1 with seawall and the progressive wave case with the same incident wave conditions without seawall to check the influence of the seawall. Fig. 21 shows the cross-shore distributions of (a) Std. and (b) mean water level at every 1/30s around t=20sec for one wave period for case (blue) and the progressive wave (red) with the same incident wave conditions. As seen in this figure, wave kinematics, i.e., Std., was really increased in the broken waves in front of the vertical wall due to the behaviors of partial standing waves. Mean water level was really decreased in the broken waves in front of the seawall which implies that the radiation stress associated with incident wave breaking is affected by the reflected waves so that setup under this partial standing waves is different form the one of pure progressive waves. Fig. 22 shows the time-varying skewness and asymmetry at X=-35cm for Case 1(blue) and progressive wave (red) with the same incident wave conditions. As seen in this figure, asymmetry was stable and was not affected by seawall and skewness was larger and unstable in front of the seawall.

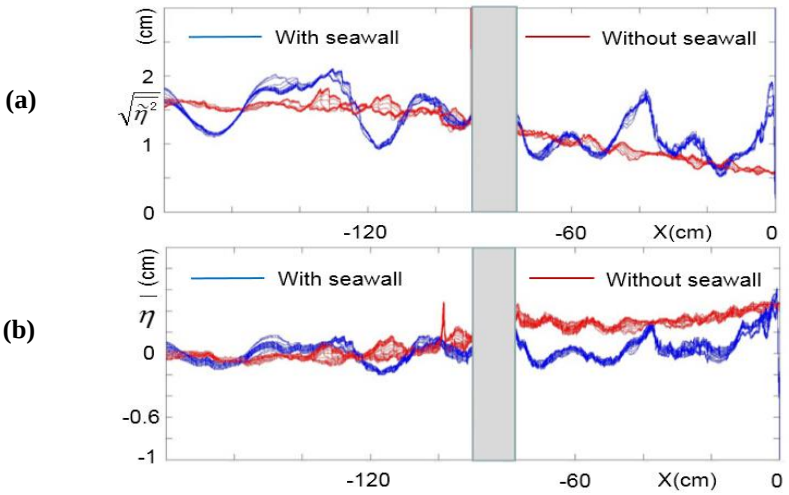

Figure 21. Cross-shore distributions of (a) Std. and (b) mean water level at every 1/30s around t=20sec for one wave period for Case1 (blue) and the progressive wave (red) with the same incident wave conditions

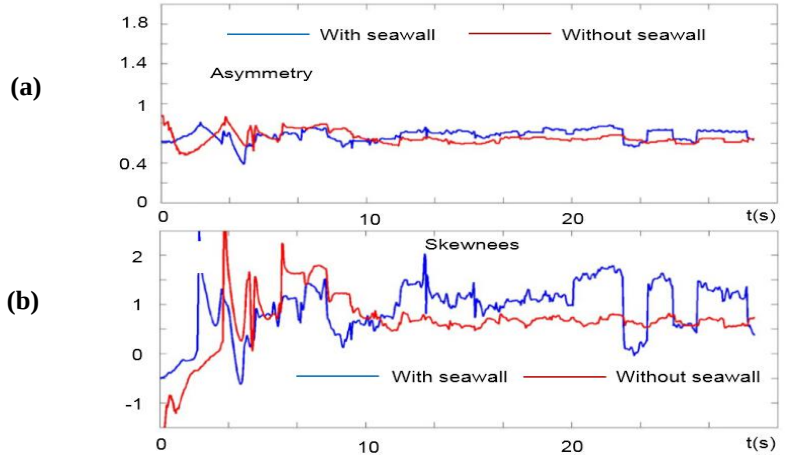

Figure 22. Time-varying (a) asymmetry and (b) skewness at X=-35cm for Case 1 (blue) and progressive wave (red) with the same incident wave conditions.

NUMERICAL ANALYSIS

Image-based measuring system successfully captured the wave characteristics in front of the seawall as high-resolution data. This section aims to further investigate the overall performance of existing widely-used breaking models under the present partial standing wave field through the comparisons of obtained experimental data and numerical results.

Model Descriptions

Time-resolving Boussinesq-type wave models are widely used to simulate the wave propagation and transformation in the surf zone. In this study, the Boussinesq equations with an improved linear dispersion relation documented by Madsen and Sorensen(1992) are used as the governing equations of the wave model for present numerical analysis.

$$\eta_t + P_x = 0 \tag{2}$$

$$P_t + \left(P^2 / d\right)_x + gd\eta_x + \psi_1 + \tau_b / \rho + F_{br} = 0 \tag{3}$$

where subscripts x and t denote differentiation with respect to space and time, $d=h+\eta$ is the total water depth, h is the still water level , η is the instantaneous water surface elevation, g is the gravity

acceleration and P is the depth-integrated velocity components. Ψ_1 is the Boussinesq terms as dispersion parameters defined by

$$\psi_1 = -(B + 1/3)h^2 P_{xxt} - BghS_{xxx} - hh_x(1/3P_{xt} + 2Bgh\eta_{xx}) \quad (4)$$

where the value of the coefficient B is determined by matching the resulting linear dispersion relation with a polynomial expansion of Stokes first order theory combined with use of Pade's approximant. By this approach the value B=1/15 was found and the resulting phase celerity was shown to be in excellent agreement with Stokes first order theory in deeper water. ρ is the mass density of water and τ_b is the near bottom shear stress due to the bottom friction.

Furthermore, F_{br} is an ad hoc momentum term to account for energy dissipation due to breaking and broken waves. Different types of breaking models have different formulations of F_{br}. In the present study, eddy viscosity type (Nwogu, 1996) and surface roller type (Shaffer et al., 1993) models are focused on. The corresponding F_{br} for eddy viscosity type breaking model is expressed as

$$F_{\mathrm{br}} = -\frac{1}{d}(\nu_t P_x)_x \quad (5)$$

where ν_t is the eddy viscosity. The rate of energy dissipation is thus governed by the magnitude of the eddy viscosity which is related to the turbulent kinematic energy, k , and a turbulent length scale, l_t. The corresponding F_{br} for surface roller type breaking model is expressed as

$$F_{\mathrm{br}} = \delta\left(c - \frac{P}{d}\right)^2\left(1 - \frac{\delta}{d}\right)^{-1} \quad (6)$$

where δ is the thickness of surface roller, c is the wave celerity. The δ in Fbr and breaking criteria is then determined by the heuristic geometrical approach.

Model Applications to Experimental Cases

Fig. 23 shows the comparison between experimental and numerical results of standard deviation of surface fluctuations, $\eta_{\mathrm{rms}} = \sqrt{\overline{\tilde{\eta}^2}}$, and mean water level, $\eta_{\mathrm{mean}} = \overline{\eta}$ for all cases. In the Figure, numerical results are when surface roller type breaking model was introduced to Boussinesq-type wave model. Parameters, i.e., η_{rms} and η_{mean}, were computed from the measured or computed time series of water surface fluctuations of the last ten wave cycles after waves reached to periodic equilibrium state. As seen in this figure, the wave setup in the breaking and broken waves in front of the seawall is overestimated while η_{rms} in front of seawall is underestimated. , i.e., dissipation of energy was overestimated. It is also noted that amplitude of periodic fluctuations of computed η_{rms} is much smaller compared to the ones of measured data. Since such cross-shore fluctuations of η_{rms} is because of formation of partial standing wave, this observed result indicates that the numerical model tends to underestimate reflected wave components.

Fig.24 shows the same comparisons as Fig.23 but the numerical predictions are based on the Boussinesq type wave model with eddy viscosity type breaking model. As seen in this figure, the existing eddy viscosity type breaking model shows similar predictive limitations of broken wave dissipation as well as wave setups compared to those by surface roller type breaking model.

CONCLUSIONS

Image-based measuring system was first successfully developed and applied to the wave flume experiments to capture the wave characteristics in front of the seawall. The behaviors of partial standing waves in front of the seawall was successfully captured. Formation of several antinodes were clearly observed in standard deviation of surface fluctuations and the mean water level also had peaks at antinodes. For the time-evolution of wave parameters, mean water level is rapidly elevated in the beginning and then go down to reach equilibrium state. While asymmetry was stable, skewness showed significant fluctuations even after the formation of steady partial standing waves. Comparisons of

obtained experimental data with and without seawall clearly showed the influence of the presence of the vertical seawall based on observed difference in cross-shore distribution of: (i) standard deviation of surface fluctuations; (ii) mean water level and (iii) skewness while clear difference was not observed in asymmetry. Seawall decreases the wave setup and increases the standard deviation of surface fluctuations and skewness in the vicinity of it. While standard deviation of surface fluctuations, mean water level and asymmetry reached to the equilibrium state, skewness was not stable even after the seawall formed partial standing waves.

Obtained experimental data was also used to check the overall performance of existing breaking models under partial standing wave field. This study focused on two widely-used breaking models, i.e., eddy viscosity type and surface roller type, attached to Boussinesq wave model. Without any calibrations/modifications, both viscosity-type and surface roller-type breaking wave models tended to overestimate the broken wave dissipation in front of the seawall.

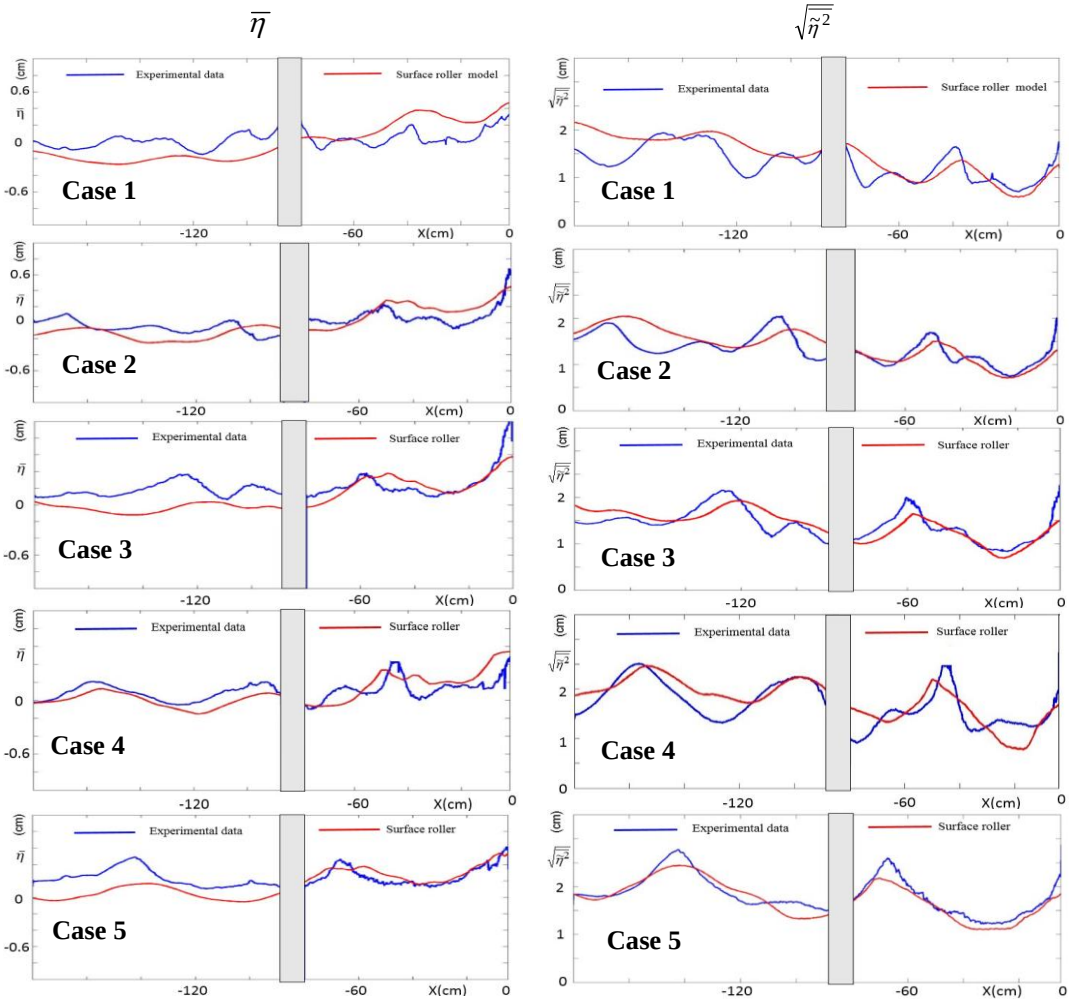

Figure 23. Comparison of measured and predicted η_{mean} and η_{rms} for all cases in this study. Predictions are based on the Boussinesq-type wave model with surface roller-type breaking model.

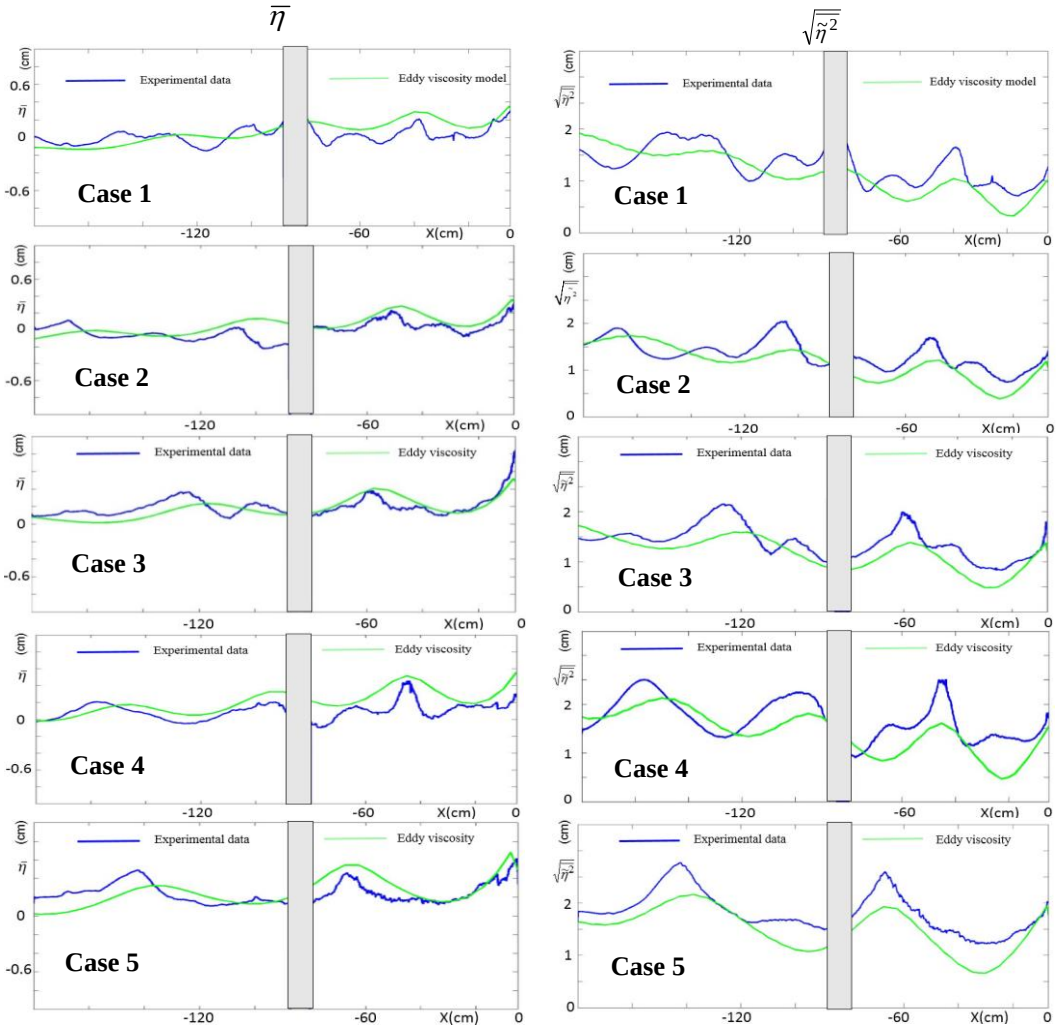

Figure 24. Comparison of measured and predicted η_{mean} and η_{rms} for all cases in this study. Predictions are based on the Boussinesq-type wave model with eddy viscosity-type breaking model.

REFERENCES

Madsen, P.A. and O.R. Sorensen. 1992. A new form of the Boussinesq equations with improved linear dispersion characteristics. Part 2. A slowly-varying bathymetry. *Coastal Engineering*, 18, 183-204.

Nwogu, O. 1996. Numerical Prediction of Breaking Waves and Currents with a Boussinesq Model, *Proceedings of 25th International Conference on Coastal Engineering*, ASCE, 4807-4820.

Schaffer, H.A., P.A. Madsen, and R. Deigaard. 1993. A Boussinesq model for waves breaking in shallow water, *Coastal Engineering*, 20, 185-202.

Tajima, Y. and S. Sato. 2010. Local concentration of slowly varying wave and current fields around the abruptly changing bottom slopes along the shore. *Proceedings of 32nd International Conference on Coastal Engineering*, ASCE. p. waves.21.